Versatile Conjugated Polymer Nanoparticles for High-Resolution O_2 Imaging in Cells and 3D Tissue Models

Ruslan I. Dmitriev,[*,†,#] Sergey M. Borisov,[*,‡,#] Heiko Düssmann,[§] Shiwen Sun,[‡] Bernhard J. Müller,[‡] Jochen Prehn,[§] Vladimir P. Baklaushev,[∥,⊥] Ingo Klimant,[‡] and Dmitri B. Papkovsky[†]

[†]School of Biochemistry and Cell Biology, University College Cork, Cork, Ireland, [‡]Institute of Analytical Chemistry and Food Chemistry, Graz University of Technology, Graz 8010, Austria, [§]Department of Physiology and Medical Physics, Centre for the Study of Neurological Disorders, Royal College of Surgeons in Ireland, Dublin 2, Ireland, [∥]Department of Medicinal Nanobiotechnology, Pirogov Russian State Medical University, Moscow 115682, Russia, and [⊥]Federal Research Clinical Centre of Federal Medical and Biological Agency of Russia, Moscow, Russia. [#]R.I.D. and S.M.B. contributed equally to this work.

ABSTRACT High brightness, chemical and photostability, tunable characteristics, and spectral and surface properties are important attributes for nanoparticle probes designed for live cell imaging. We describe a class of nanoparticles for high-resolution imaging of O_2 that consists of a substituted conjugated polymer (polyfluorene or poly(fluorene-*alt*-benzothiadiazole)) acting as a FRET antenna and a fluorescent reference with covalently bound phosphorescent metalloporphyrin (PtTFPP, PtTPTBPF). The nanoparticles prepared from such copolymers by precipitation method display stability, enhanced (>5−10 times) brightness under one- and two-photon excitation, compatibility with ratiometric and lifetime-based imaging modes, and low toxicity for cells. Their cell-staining properties can be modulated with positively and negatively charged groups grafted to the backbone. The "zwitter-ionic" nanoparticles show high cell-staining efficiency, while their cell entry mechanisms differ for the different 3D models. When injected in the bloodstream, the cationic and anionic nanoparticles show similar distribution *in vivo*. These features and tunable properties make the conjugated polymer based phosphorescent nanoparticles a versatile tool for quantitative O_2 imaging with a broad range of cell and 3D tissue models.

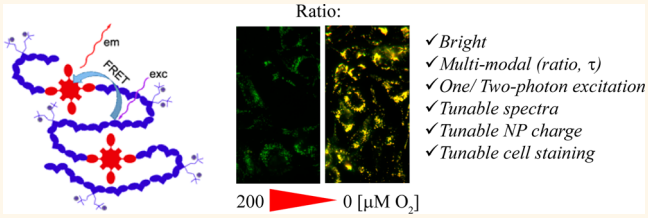

KEYWORDS: 3D tissue model · cell and tissue oxygenation · cell-penetrating nanoparticle probe · conjugated polymer · imaging · molecular oxygen · phosphorescence quenching

In the last years, quenched phosphorescence oxygen sensors proved to be efficient analytical tools in life science areas, from marine to cancer biology.[1,2] Optical sensing of O_2 enables various measurement formats and applications: these include planar optodes for 2D visualization of O_2,[3,4] fiber-optic (micro)sensors for point measurements,[5] sensor paints for imaging on uneven surfaces,[6] and nanosensors and probes.[7−9] Nanosensors are attractive due to their small size and ability to collect information from small objects such as cells and cellular components, and they respond in real time to alterations in O_2 concentration. In contrast to small molecule and supramolecular probes, the indicator dye in the nanosensors is shielded from the environment with a polymeric shell resulting in more stable response and low cross-sensitivity to other species. Although nanosensors can be used in bioreactors like solid-state and fiber-optic sensors, biological screening and fluorescence microscopy[10] remain their primary application fields. Nanosensors are compatible with conventional fluorescence and laser-scanning (confocal, one- and two-photon) microscopes.[11] Two-photon microscopy becomes increasingly popular due to its high resolution, low photobleaching and background signals, and deep (up to 1 mm) light penetration. Imaging O_2 in mammalian tissue under two-photon excitation is of particular interest.[12−16] Although many two-photon excitable dyes have been reported,[17,18] there is a clear lack of dedicated luminescent probes for various analytes.[14,19−21] Brighter probes, *e.g.*, based on asymmetrical porphyrins,[22] can provide better signal-to-noise ratio and be used at lower concentrations and with better performance.

* Address correspondence to r.dmitriev@ucc.ie, sergey.borisov@tugraz.at.

Received for review February 3, 2015 and accepted April 10, 2015.

Published online April 10, 2015
10.1021/acsnano.5b00771

Luminescent nanosensors typically use indicator dye(s) embedded in an organic (polymer) or inorganic (*e.g.*, silica) matrix.[23] Their surface can be functionalized to improve solubility in water, cell penetration, and other characteristics. Popular O_2 indicators are Pt(II)− and Pd(II)−porphyrins and their analogues, Ru(II)−polypyridyl, Ir(III)−, and Pt(II)−cyclometalated complexes.[24] Their long luminescence decay times (1−1000 μs) allow lifetime-based O_2 sensing which can be realized by phase or time-resolved fluorometry and time-correlated single photon counting (TCSPC).[25,26] For imaging applications ratiometric intensity mode is also useful,[27,28] requiring only a set of two filters in front of the detector or a RGB camera.[29,30] For ratiometric read-out, an O_2-insensitive fluorophore should be incorporated into the sensor along with the indicator.[28] The common problem of nanosensors is leaching and/or bleaching which usually differ for the two luminophores and result in drift of O_2 calibration. Covalent immobilization helps to avoid leaching of the indicators; however, only a few such systems have been reported so far.[31−34]

Conjugated polymers are promising for application in organic optoelectronics and photovoltaics[35−37] and sensing and imaging applications.[38−40] Many such probes have been reported; however, O_2 sensing applications are quite rare.[31,34,41] Their main challenges include water solubility, cell penetration and biodistribution in cells, and operational and storage stability. We and others showed that nanoparticle O_2 probes often have poor in-depth staining of 3D cell models.[42−44] For the growing area of biomaterials, imaging nanosensors with improved performance and tunable structure and characteristics are needed.[45]

Here, we present a new nanosensor platform based on conjugated polymers acting as matrix, light-harvesting antenna, and reference, copolymerized with O_2 sensing indicator dye, and grafted with charged groups providing cell and tissue penetration and stability in aqueous solutions. These nanoparticles allow ratiometric intensity and phosphorescence lifetime-based O_2 detection, under one or two-photon excitation, in the visible or near-infrared spectral ranges. We demonstrate that flexible design and charge characteristics facilitate efficient staining and imaging of various cancer cell and tissue models, with >5−10 times higher brightness and improved performance of O_2 imaging.

RESULTS AND DISCUSSION

Preparation of the Conjugated Polymers and Nanoparticles. The conjugated polymers can be conveniently prepared *via* Suzuki−Miyaura reaction from commercially available diboronic acids and dibromo-substituted building blocks. Altering the nature and ratio of the building blocks allows tuning spectral properties of the resulting polymers, lipophilicity, introduction of an O_2 indicator, and charged groups. We synthesized two series of luminescent polymers, which significantly differ in their spectral properties. The first (designated as SI, Figure 1) uses only fluorene-based building blocks. The blue-emitting polyfluorene acts as energy donor for platinum(II) *meso*-bis(pentafluorophenyl)bis-(4-bromophenyl)porphyrin ($PtTFPPBr_2$) copolymerized with it. In the second series (designated as SII), 2,1,3-benzothiadiazole units alternate with the fluorene producing a polymer with bathochromic shift of the absorption and fluorescence spectra. In SII, a near-infrared (NIR)-emitting benzoporphyrin precursor $PtTPTBPtBu_4Br_4$ was grafted to the polymer and used as an energy acceptor. The molecular weight of the resulting copolymers typically varied between 10 and 40 kDa (Table S1, Supporting Information).

Conjugated polymers prepared by Suzuki coupling do not contain charged groups. These are introduced in the second step *via* alkylation of (*N*,*N*-dimethylamino)propyl- (positive charge) or/and hydrolysis of the methylpropionate (negative charge) groups in the fluorene (Table 1). For simplicity, the following nomenclature was chosen: series (I or II) and number of charged groups, *e.g.*, SI-0.2$^+$ meaning "co-polymerized $PtTFPPBr_2$ with *N*,*N*,*N*-trimethylpropylammonium-substituted fluorene". All charged copolymers were soluble in organic solvents except for SI-0.3$^+$/0.1$^-$, which was not suitable for preparation of nanoparticles. Further, we prepared the nanoparticles from copolymers using the "precipitation" technique[46] by dissolving the polymer in a "good" solvent (tetrahydrofuran/acetone mixture) and rapidly adding an excess of water to it.

Physical and Photophysical Properties of the Nanoparticles. Table 1 summarizes physical properties of the resulting nanobeads. Their size of about 50 nm is similar to the nanoparticles reported before,[46−48] being small enough for intracellular measurements. As is visible from the transmission electron microscopy (TEM) image (Figure 1C), the nanoparticles displayed almost spherical shape. The size estimated from the TEM measurements (Figure S1, Supporting Information) corresponds well with the results obtained in dynamic light scattering (DLS) experiments (Table 1). The charge in water depends on the nature and density of the charged groups introduced in the polymer. Thus, the nanoparticles bearing quaternary ammonium groups had $Z_{potential}$ = +34 mV (Table 1) and with the propionic acid moieties $Z_{potential}$ = −23 mV. $Z_{potential}$ did not change upon substitution of the fluorene moiety with benzothiadiazole. For the particles containing both quaternary ammonium and propionic acid moieties ("zwitter-ionic") $Z_{potential}$ strongly depended on pH (Figure S2, Supporting Information).

Figure 2 shows the excitation and emission spectra of the nanoparticles of both series. The first series is efficiently excitable with UV/violet light *via* the

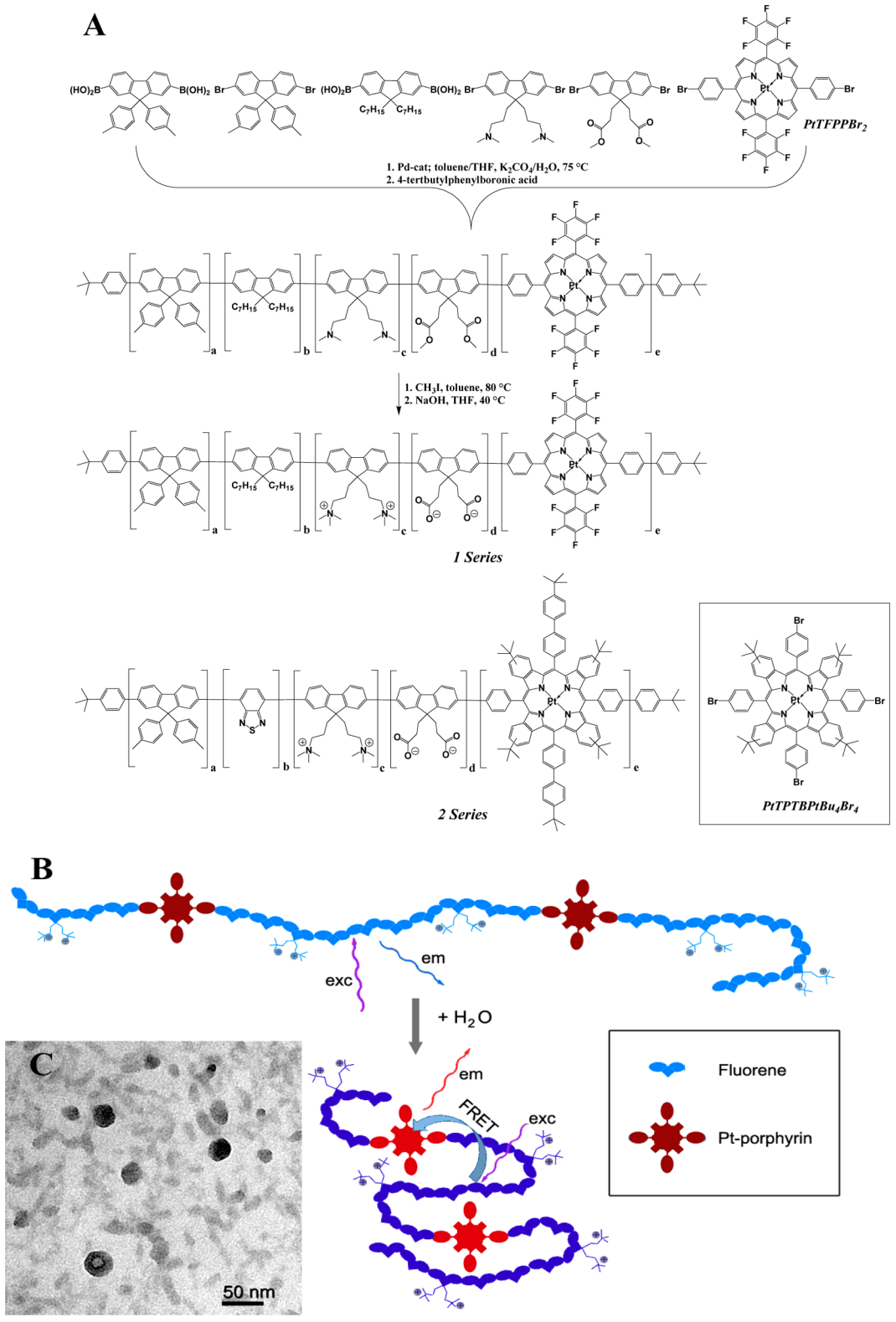

Figure 1. Synthesis scheme and structure of the O_2-sensitive conjugated polymers (A), their conformation in organic solvent and in nanoparticle form after precipitation with water (B), and TEM image of the resulting nanoparticles (SI-0.15$^+$/0.05$^-$) (C).

polyfluorene backbone (Figure 2A) acting as an antenna. Direct excitation of the porphyrin at Q-bands (500−550 nm) was much less efficient. Residual blue emission from polyfluorene and strong red phosphorescence from copolymerized Pt(II)−porphyrin can be seen in Figure 2C. Intensities of both emission signals were optimized and determined by the ratio of the monomers[31] which was 0.8 mol % or ~2% weight of the

porphyrin in the resulting polymer. A higher amount of the porphyrin resulted in the materials having only phosphorescence, whereas at lower concentrations of the acceptor FRET was less efficient and highly efficient fluorescence from polyfluorene was observed (not shown). Comparison with a spectrally similar probe MM2 (PtTFPP and 10 wt % of polyfluorene in Rl-100 polymer) at the same concentration (1.3 μg/mL) revealed much brighter phosphorescent signals from the copolymer nanoparticles. The emission of copolymerized Pt(II)-porphyrin is red-shifted by 14 nm compared to PtTFPP, which we attribute to extended π-conjugation of the former.

Introduction of electron-deficient benzothiadiazole into the polymer backbone results in the bathochromic shift of the excitation peak of SII compared to the SI (Figure 2B). SII shows green residual emission from poly(fluorene-*alt*-benzothiadiazole) and NIR emission from Pt(II)– benzoporphyrin (Figure 2D). Again, FRET from the conjugated polymer to the porphyrin was found to be very efficient in nanoparticles. Compared to the similar probe $NanO_2$–IR,[49] the new nanoparticles benefit from higher brightness of phosphorescence upon excitation with blue light. Under direct excitation of Pt(II)–benzoporphyrin with red light the signals are comparable for both probes (Figure 2D). In the copolymers we also observed bathochromic shifts for Pt(II)-porphyrin emission and excitation Q bands (Table 2).

Properties of the conjugated polymers in organic solvent and in aqueous suspension of nanoparticles

TABLE 1. Physical Properties of the Nanoparticles in Water, 25 °C

bead name	Z_{av} (nm)	PDI	$Z_{potential}$ (mV)
SI-0.1^{+}/0.1^{-}	47	0.231	+34
SI-0.2^{+}/0.2^{-}	28	0.288	+28
SI-0.05^{+}/0.15^{-}	112	0.124	+34
SI-0.1^{+}/0.3^{-}	59	0.214	+29
SI-0.15^{+}/0.05^{-}	38	0.230	+33
SI-0.2^{+}	35	0.249	+34
SI-0.2^{-}	56	0.192	−23
SII-0.2^{+}	52	0.129	+33
SII-0.2^{-}	50	0.09	−23

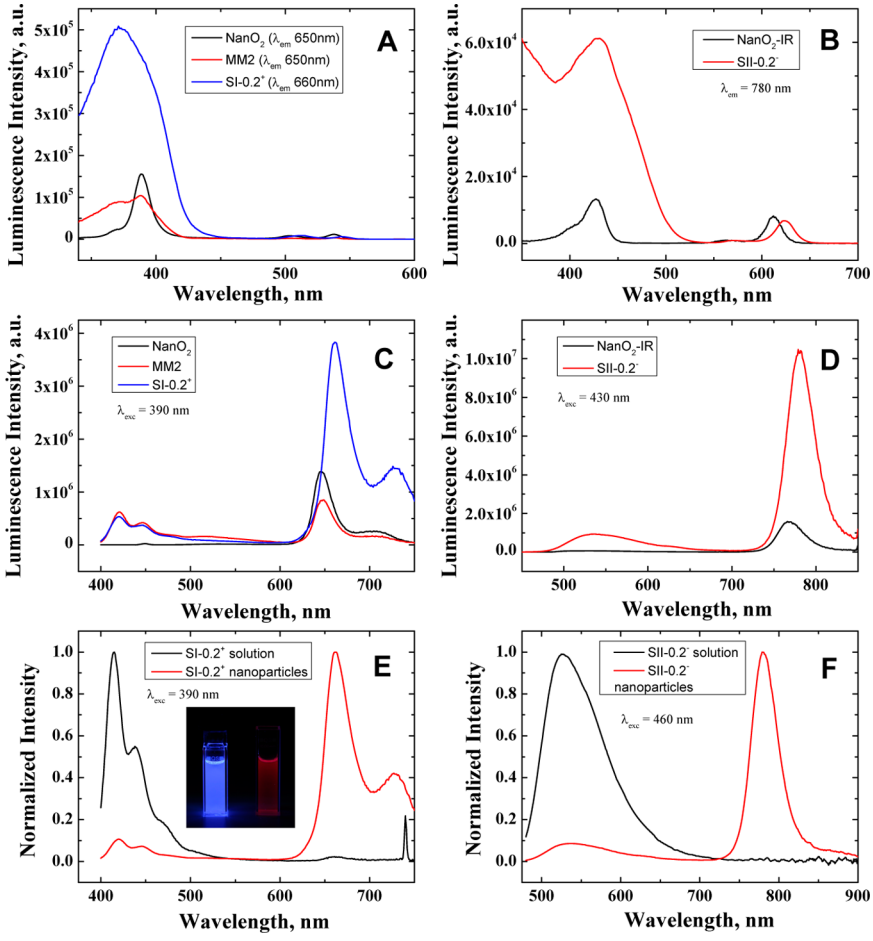

Figure 2. Excitation (A, B) and emission (C, D) spectra for the nanoparticles from SI (A and C) and SII (B and D) compared to the spectra of previously reported nanoparticles used in the same concentration (1.3 μg/mL for SI, $NanO_2$ and MM2 and 2.8 μg/mL for SII and $NanO_2$–IR). The emission spectra for the solution of the polymer in THF and for the nanoparticles in water are compared (E and F for SI and SII, respectively). The inset shows the emission of the polymer (left) and nanoparticles (right) under excitation with a UV lamp (366 nm, SI series). All of the spectra were acquired at anoxic conditions at 25 °C.

TABLE 2. Photophysical Properties of the Nanoparticles in Anoxic Water and the Properties of the Previously Reported Nanoprobes

bead name	λ_{max}exc/em (nm)	Φ (porphyrin emission)[b] (%)	Φ (conj polymer emission)[b] (%)	τ (phosphorescence) (μs)	I_0/I (porphyrin emission), 25 °C
SI-0.1$^+$/0.1$^-$	371, 400(sh)/421 (fl)[a], 447 (fl), 661 (phos)	4.2	1.4	65.4[d]	3.15
SI-0.2$^+$/0.2$^-$		2.5	0.8	58[d]	3.94
				64 (81%)[e]	
				27 (19%)[e]	
SI-0.05$^+$/0.15$^-$		3.1	1.2	63[d]	2.98
SI-0.1$^+$/0.3$^-$		2.2	0.8	47[d]	3.08
				54.4 (80%)[e]	
				22.6 (20%)[e]	
SI-0.15$^+$/0.05$^-$		4.1	1.5	62[d]	4.35
SI-0.2$^+$		3.8	1.3	58[d]	3.32
SI-0.2$^-$		4.3	1.2	58[d]	3.35
MM2	371, 389/421 (fl), 447 (fl), 647 (phos)	9.7	7.8	82[d]	3.07
$NanO_2$	389, 505, 538/647 (phos)	18		81[d]	
SII-0.2$^+$	431, 624/536 (fl), 782 (phos)	16 (17.7)[c]	1.6	41 (83%)[e]	2.1
				15 (17%)[e]	
SII-0.2$^-$		11 (14.2)[c]	2.8	40 (82%)[e]	2.05
				14 (18%)[e]	
$NanO_2$—IR	427, 612/769 (phos)	36[c]		61[d]	3.5

[a] fl = fluorescence, phos = phosphorescence; sh = shoulder. [b] Excitation in the conjugated polymer band. [c] Excitation in the Q-band (620 nm) of the Pt(II)—porphyrin. [d] Monoexponential decay fit. [e] Biexponential decay fit; the parentheses indicates the relative contributions of each component.

were then compared (Figure 2E,F). Surprisingly, practically no FRET was observed for the dissolved conjugated polymer, which only emitted blue (SI, Figure 2E) or green light (SII, Figure 2F) under anoxic conditions. Thus, close proximity of multiple antenna chains to the porphyrin acceptor is necessary, which is only achieved when the polymer "folds" to form compact spherical nanoparticle structures as shown in Figures 1C and Figure S1 (Supporting Information), confirmed by DLS and TEM measurements. This folding is reproducible and results in similar FRET efficiency for different batches of the particles obtained *via* precipitation (Figure S3, Supporting Information). The nanoparticles remained stable upon storage at 4 °C over 6 month period (not shown).

We next evaluated photophysical properties of nanoparticles in solution. Luminescence decays are shown in Figure 3. Comparison of SII in THF (soluble copolymers) and in water (nanoparticle form) confirms efficient quenching of the antenna fluorescence with decay time drastically reduced from 3.2 ns to about 170 ps (Figure 3A). The Pt(II)—porphyrin showed microsecond decay times (phosphorescence), being practically the same for the positively and the negatively charged conjugated copolymers. The shapes of decays slightly deviated from monoexponential (Figure 3B,C) and indicated shorter lifetimes than for PtTFPP and PtTPTBPF in Rl-100 nanoparticles ($NanO_2$ and $NanO_2$—IR, respectively, Table 2). Shorter decay time in the conjugated polymer may indicate some quenching of the phosphorescence by the polyfluorene (or poly(fluorene-*alt*-benzothiadiazole) backbone. In fact, triplet states of the conjugated polymers can be close in energy to the porphyrins.[50] Indeed, the quantum yield of Pt(II)—porphyrin in copolymers was decreased, 2.2—4.3% for SI nanoprobes, contrasting ~18% for PtTFPP embedded in Rl-100 beads (Table 2, $NanO_2$) and ~10% for the MM2 probe (10% wt. of polyfluorene, 1 wt % of PtTFPP in Rl-100). The same was also observed for the SII nanobeads, but quantum yields only decreased 2—3-fold and remained rather high (>10%), possibly due to lower quenching effect of poly(fluorene-*alt*-benzothiadiazole) on Pt(II)—benzoporphyrin. Collectively, the efficient excitation *via* the conjugated polymer antenna compensates for decreased quantum yields and makes the nanobeads very promising for lifetime imaging microscopy (PLIM) or ratiometric detection of O_2.

In aqueous solutions, SI and SII nanoparticles displayed adequate sensitivity over the whole physiological range (0—20 kPa O_2) (Figure 4). Ratiometric response was similar to previously described MM2 and PA2 nanosensors.[42,47] Stern—Volmer plots were slightly curved and fitted well with the two-site model.[51]

Staining of Monolayer (2D) Cell Culture with Nanoparticles. Unlike the "dye-doped" nanoparticles,[42,47] the new copolymers SI and SII all consist of chromophores (antenna backbone and O_2-sensitive dye), but due to the introduced charged groups they have similar Z-potentials (Table 1). With mouse embryonic fibroblast (MEF) cells we observed different cell staining depending on the nanoparticle charge: SI-0.1$^+$/0.1$^-$ and SI-0.2$^+$ displayed efficient internalization upon 16 h incubation while negatively charged SI-0.2$^-$ displayed more than 10-fold lower intensity signals

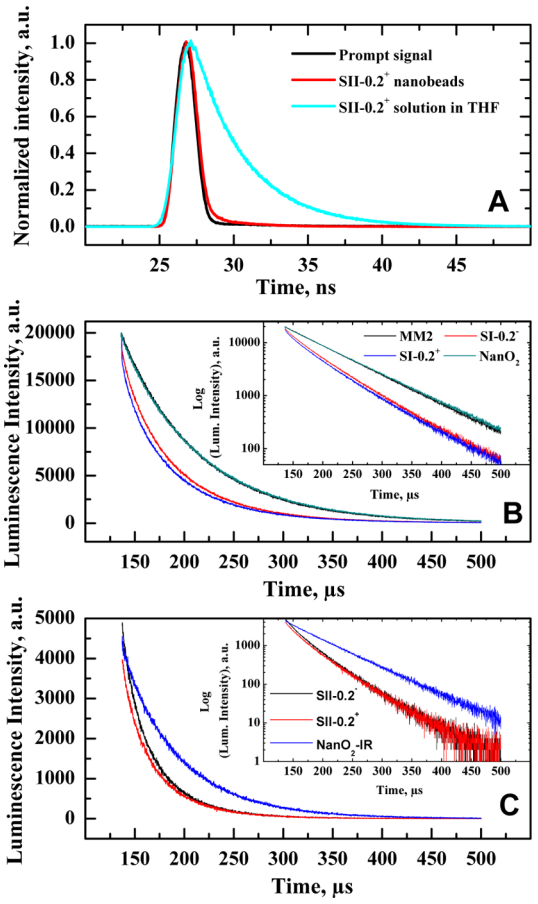

Figure 3. Luminescence intensity decay curves monitored for the fluorescence (λ_{exc} 453 nm, λ_{em} 540 nm) of SII (A) and phosphorescence of SI (B; λ_{exc} 392 nm, λ_{em} 655 nm), and SII (C; λ_{exc} 392 nm, λ_{em} 770 nm) as well as in the previously reported nanoparticles MM2, $NanO_2$ and NanO2-IR. All of the experiments were conducted in deoxygenated solutions.

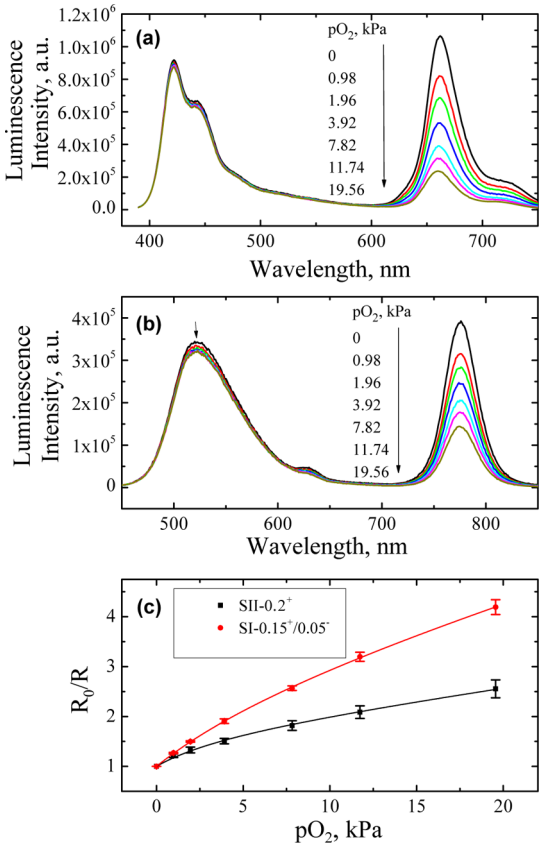

Figure 4. Uncorrected emission spectra for aqueous dispersion of SI-0.15^{-}/0.05^{+} (a; λ_{exc} = 380 nm) and SII-0.2^{+} (b; λ_{exc} = 435 nm) nanoparticles at different pO_2 in water (25 °C). (c) Corresponding calibration plots for luminescence intensity ratio in the absence (R_0) and presence (R) of oxygen; $R = I_{661\ nm}/I_{422\ nm}$ for SI-0.15^{-}/0.05^{+} and $I_{776\ nm}/I_{525\ nm}$ for SII-0.2^{+}.

than SI-0.2^{+} (Figure 5A). The zwitter-ionic nanoparticles demonstrated highest cell loading (compare phosphorescence intensity counts at 20 μg/mL cell loading concentration). Both SI-0.1^{+}/0.1^{-} (Figure 5) and SI-0.2^{+} (not shown) displayed colocalization of reference (421 and 447 nm emission) and O_2 (661 nm emission) dyes in the cells when excited at 405 nm. This confirms that inside the cells nanoparticles remain stable and FRET between antenna and O_2 dye occurs. Intracellular distribution was similar to MM2 and PA2 nanoparticles, localizing to pool of endosomes and lysosomes (pH range from 7.4 to 4.5), and photostability (not shown) was sufficient for PLIM measurements. Stained cells showed response to O_2, in ratiometric-intensity and lifetime detection modes (Figure 5C,D).

The structure of nanoparticles includes a high number of aromatic (π-conjugated) groups which potentially can mediate their toxicity for living cells, *e.g.*, through photoinduced generation of reactive oxygen species. However, we did not see direct toxic effects on cells appearance after 16 h exposure and post illumination with 405 nm laser (not shown). We therefore evaluated toxicity of nanoparticles with different charges on cultured cells after 16 h exposure using three different assays: membrane integrity assay, total cellular ATP, and analysis of extracellular acidification at rest and upon metabolic stimulations, informing on overall cell bioenergetics status (Figure S4, Supporting Information). No significant effects were observed, except for the zwitter-ionic nanoparticles, which had a slight effect on extracellular acidification (indicator of glycolysis) at high concentration 20 μg/mL (Figure S4C, Supporting Information). This can be considered in future physiological experiments. Overall, this data indicate that nanoparticles have minimal effect on cell viability and are compatible with physiological measurements.

Two-Photon Imaging Properties of Nanoparticles. Conjugated polymers possess much more efficient multiphoton absorption than conventional dyes.[52,53] Together with efficient FRET to Pt(II)−porphyrin, this prompted us to evaluate two-photon excitation properties of the nanoparticles. Loaded with nanoparticles and fixed with paraformaldehyde MEF cells were analyzed on a two-photon fluorescence microscope (Figure 6). Similar to one-photon microscopy (Figure 5), we observed intracellular localization of the nanoparticles

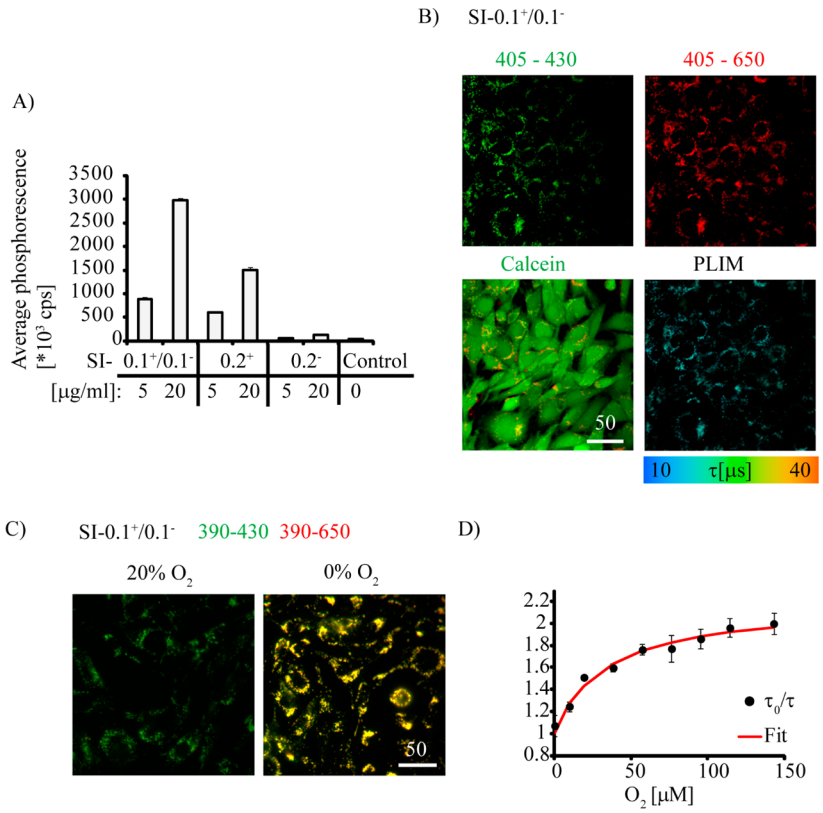

Figure 5. (A) Staining efficiency of MEF cells with copolymer nanoparticles, measured on a Victor2 microplate reader (delay time t_1 = 20 μs) and shown as the average phosphorescence counts. (B) Characteristic staining pattern for nanoparticles observed on laser-scanning PLIM microscope, with 405−430 showing the fluorescence image of reference dye and 405−650 showing the image of O_2-sensitive dye. Bottom: counter-staining with Calcein Green dye (green) confirming intracellular localization and false-color PLIM image with scale of phosphorescence lifetimes. (C) Ratiometric intensity imaging of nanoparticles (SI-0.1$^+$/0.1$^-$) in MEF cells exposed to different O_2 at 37 °C and treated with inhibitor of respiration (antimycin A, 10 μM). Combined polyfluorene (390−430, green) and Pt(II)−porphyrin (390−650, red) intensity images are shown. (D) Phosphorescence lifetime O_2 calibration of nanoparticles (SI-0.1$^+$/0.1$^-$) in MEF cells shown as Stern−Volmer plot (fitting by two-site model). N = 3. Scale bar is in micrometers.

and strong colocalizing signals of polyfluorene and Pt(II)−porphyrin under 750 nm excitation (not shown). When comparing MM2, SI-0.1$^+$/0.1$^-$ and SI-0.2$^+$ under one-photon excitation (Figure 6A) we saw similar brightness at equal loading concentrations (5 μg/mL, 16 h). However, under two-photon excitation, we observed >5-fold increase of emission intensity, over a broad range of excitation wavelengths, especially for SI-0.1$^+$/0.1$^-$ (Figure 6B). This confirms that copolymer nanoparticles possess significantly increased two-photon cross section due polyfluorene and its antenna effect. Compared to MM2 and PA2 probes containing 10% (w/w) of the polyfluorene,[42,47] two-photon emission of SI was much higher (Figure 6C). Similar to the two-photon dendritic probe with Coumarin 343 antenna,[54] the dependence of emission from laser power was almost quadratic for antenna (fluorene) and close to linear for Pt(II)−porphyrin (Figure 6D).

Two-photon excitability of SII-0.2$^+$ nanoparticles (Figure S5, Supporting Information) was also evaluated by analyzing the emission of antenna dye at 520 nm and compared to polyfluorene-based SI-0.1$^+$/0.1$^-$ and SI-0.2$^+$ (Figure S5C, Supporting Information). Considering the significantly more efficient NIR phosphorescence of the Pt(II)−benzoporphyrin (Figure 2D) compared to the residual emission from poly(fluorene-*alt*-benzothiadiazole), it can be concluded that the new material is one of the most efficient NIR probes for imaging of O_2 under two-photon excitation.

Overall, copolymer nanoparticles are much brighter than nanoparticle probes of the previous generation (MM2 and PA2). They also display more uniform intracellular distribution facilitating higher quality intracellular O_2 measurements, particularly in two-photon mode. This can be performed both under PLIM and ratiometric-intensity modes. However, the latter method is less preferred as it can be affected by different efficiency of light penetration and scattering for reference and O_2 dyes.[13]

Charge of Zwitter-ionic Nanoparticles Affects Intracellular Distribution, Cell Entry Kinetics, and Staining of 3D Cancer Models. Tuning of overall charge and Z-potential is another important feature of the copolymer nanoparticles. We found two times higher staining of MEF cells with zwitter-ionic nanoparticles (SI-0.1$^+$/0.1$^-$) over a 3 h period than with positively charged (SI-0.2$^+$)

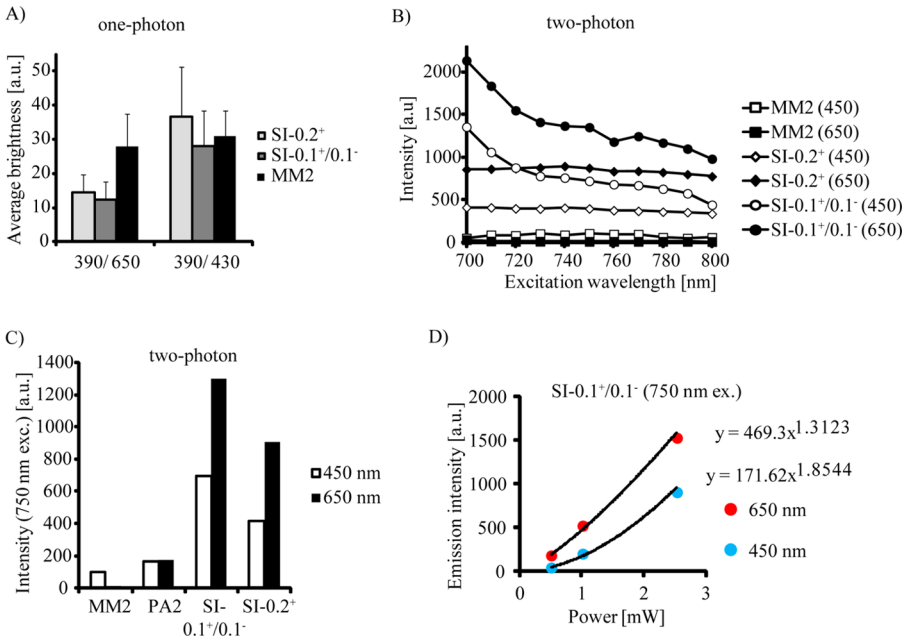

Figure 6. Evaluation of two-photon excitation properties of nanoparticles. (A) Average comparison of brightness of MM2, SI-0.1$^+$/0.1$^-$, and SI-0.2$^+$ in fixed MEF cells under one-photon excitation. (B) Two-photon excitation spectra of MM2, SI-0.1$^+$/0.1$^-$, and SI-0.2$^+$ in fixed MEF cells normalized to laser power (mW at the sample), with 450 nm indicating emission of reference and 650 nm indicating the O_2 dye. (C) Comparison of two-photon excitation for MM2, PA2, SI-0.1$^+$/0.1$^-$, and SI-0.2$^+$ under 750 nm excitation. (D) Dependence of emission intensity on the intensity of excitation light for reference (450 nm) and Pt−porphyrin (650 nm) dyes in SI-0.1$^+$/0.1$^-$ nanoparticles at low laser power (milliwatts at the sample).

nanoparticles (data not shown). We reasoned that this is due to the differences in the intracellular uptake mechanism caused by the different charge distribution on nanoparticles. Thus, SI-0.1$^+$/0.1$^-$ and SI-0.2$^+$ demonstrated different degrees of colocalization (Pearson's correlation coefficient) with caveolin-1 and clathrin markers of different endocytosis pathways (Figure S6, Supporting Information). Indeed, the balance of positively and negatively charged groups in zwitter-ionic nanoparticles also affected cell internalization. For zwitter-ionic beads SI-0.1$^+$/0.1$^-$, SI-0.2$^+$/0.2$^-$, SI-0.05$^+$/0.15$^-$, SI-0.1$^+$/0.3$^-$ and SI-0.15$^+$/0.05$^-$ (Tables 1 and 2) having sizes of 28−112 nm, using immunofluorescent costaining against markers of the two principal endocytosis cell entry pathways (caveolin-1 for macropinocytosis and clathrin heavy chain for clathrin-mediated uptake)[55,56] we observed very different patterns of intracellular localization (Figure S6B, Supporting Information). SI-0.1$^+$/0.1$^-$ showed highest degree of colocalization with clathrin, suggesting it as main cell entry pathway, in MEF cells. Positively charged SI-0.2$^+$ showed weaker colocalization with clathrin and caveolin-1. All of the nanoparticles did not colocalize with mitochondria; therefore, recycling endosomes can be regarded as their main destination. We also found that different numbers of charged groups on nanoparticles affect cell-staining kinetics (Figure S6C, Supporting Information). The highest efficiency was found for SI-0.1$^+$/0.1$^-$ (48 nm size, half-saturation in ~3 h), which is significantly faster than for any known O_2-sensitive nanoparticles.[9,30,57,58]

3D cell models such as spheroids are attractive *in vitro* models of cancer and stem cell development but their in-depth staining with probes is challenging.[45] We evaluated charged copolymer nanoparticles with two models: aggregates of nondifferentiated PC12 cells (size 50−100 μm)[59] and spheroids of HCT116 cells (Figure 7A−C). In contrast to the cationic MM2 probe, which mostly produced patchy staining of PC12 cells, all negatively charged and zwitter-ionic copolymers efficiently internalized in the cells across the whole volume of aggregates (over 16 h time), as evidenced by Calcein Green costaining. Cationic only SI-0.2$^+$ and SI-0.15$^+$/0.05$^-$ showed slight aggregation. Preformed spheroids made from HCT116 cells (sHCT116) having sizes >50 μm were impossible to completely stain in depth with any tested probe including Calcein Green (Figure 7B). This is probably due to presence of dead cells within the spheroid, as evidenced by CellTox Green and propidium iodide staining (not shown). Still, copolymer nanoparticles showed staining of the surface (down to 30−40 μm) layers. In contrast to the PC12 cell model, with sHCT116 cationic SI-0.2$^+$ showed the most efficient staining (Figure 7C). Interestingly, zwitter-ionic samples demonstrated different performance with sPC12 and sHCT116 aggregates, reflecting reliance on different cell entry pathways (Figure 7A,C). Thus, one can clearly see specificity and tunability of intracellular transport of copolymer nanoparticles: zwitter-ionic nanoparticles are optimal for PC12 and cationic for sHCT116 cells.

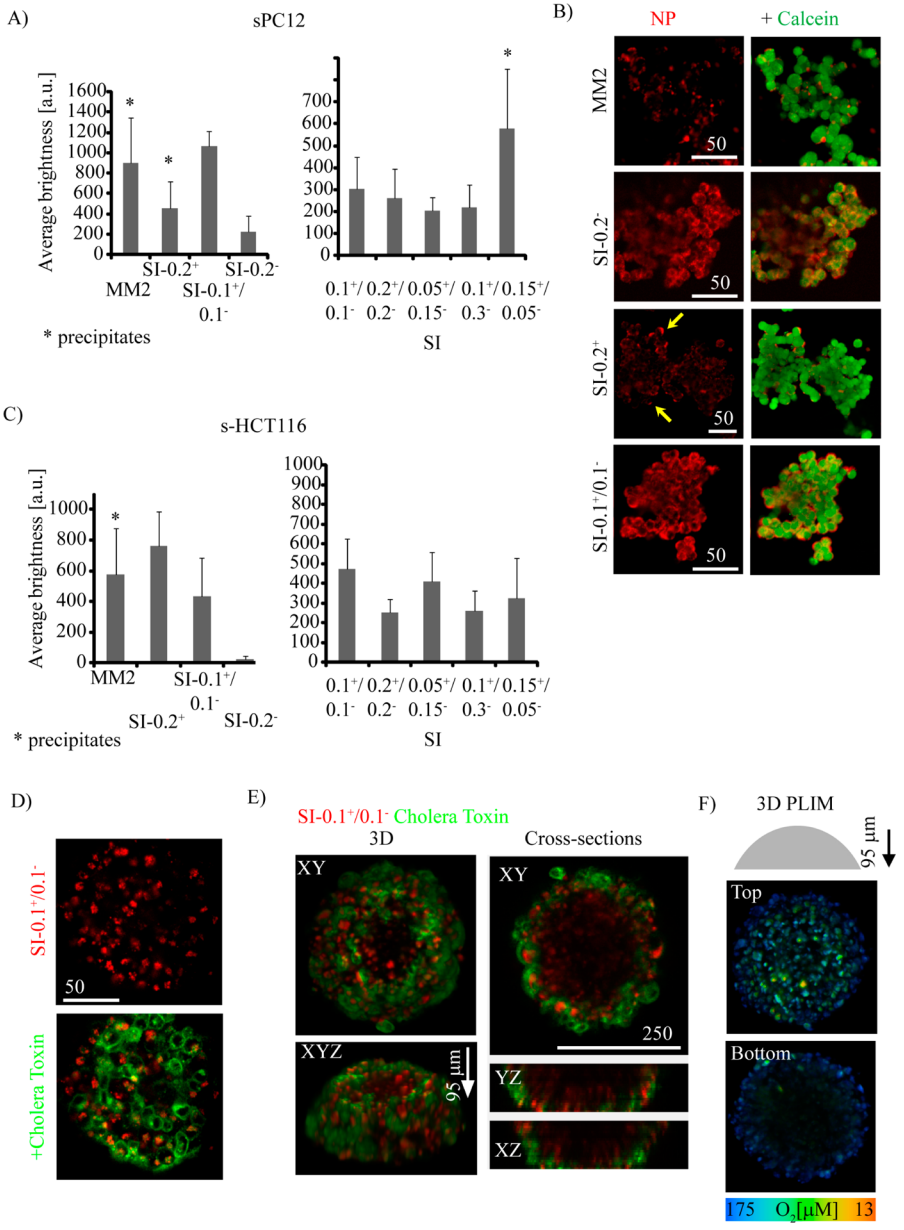

Figure 7. Staining of 3D tissue models with nanoparticles of different charge. (A–C) One-photon confocal microscopy analysis of average staining efficiency of multicellular aggregates PC12 (A, B) and spheroids HCT116 (C) with nanoparticles at 5 μg/mL, 16 h. (B) Example of stained sPC12 with nanoparticles costained with Calcein Green (1 μM, 0.5 h). Arrows indicate aggregates. N = 12. (D) Intracellular localization of SI-0.1^{+}/0.1^{-} (added at 5 μg/mL at the spheroid formation) in sHCT116. Sample was co-stained with Cholera toxin, subunit B-Alexa Fluor 488 conjugate (2.5 μg/mL, 4 h). (E) 3D reconstruction of SI-0.1^{+}/0.1^{-} in spheroids HCT116 revealed by one-photon confocal microscopy. (F) 3D reconstruction of O_2 distribution by PLIM for the same spheroid. Scale bar is in micrometers.

The inability of nanoparticles to show efficient in-depth staining of spheroid cell models over short periods of time (16 h) was noted before[43,59] and perhaps reflects intrinsic limitation of moderate size nanoparticles (30–100 nm size) to diffuse across multiple cell volumes. However, compared with $NanO_2$, the continuous staining method (when nanoparticles are present in solution during formation of spheroids)[43] allowed better in-depth distribution of copolymers, without any visible patches and inside the cells. We found that copolymer nanoparticles can efficiently accumulate inside the HCT116 cells and reside in macropinosomes and acidic organelles (Figure S7, Supporting Information). Figure 7D,E shows that uniform staining of 50–300 μm size spheroids can be achieved, with intracellular localization of nanoparticles, allowing much deeper staining than with small molecule Calcein Green. This allows for oxygenation 3D PLIM maps to be reconstructed for living spheroids (Figure 7F). Collectively, copolymer nanoparticles provide efficient staining of 3D cell models, which supports their high usability in one- and two-photon

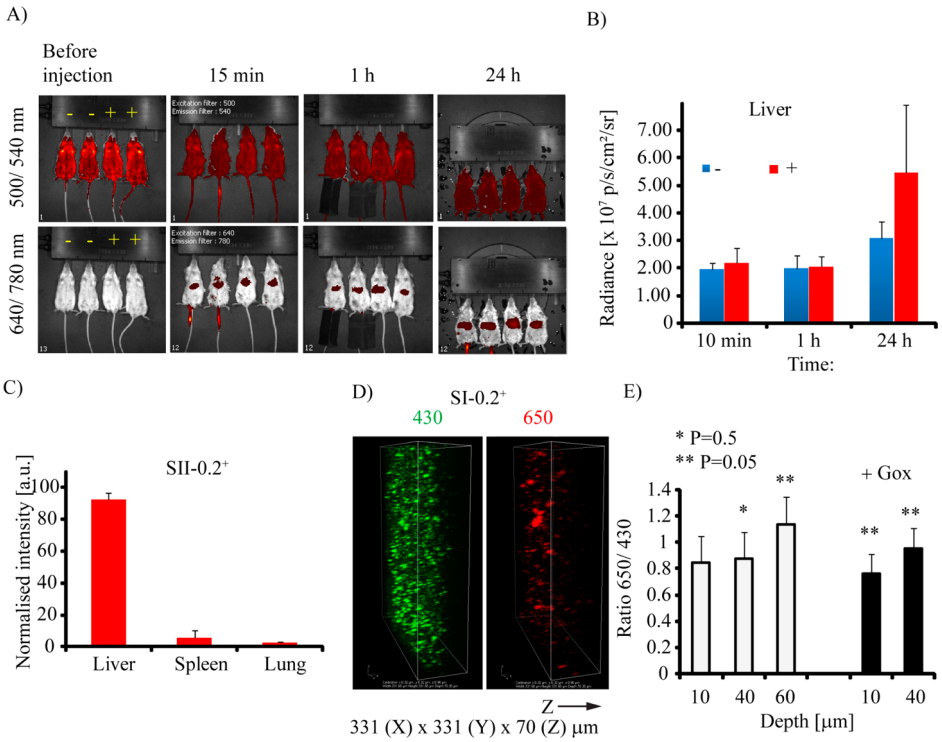

Figure 8. (A) In vivo imaging of nanoparticles SII-0.2$^-$ and SII-0.2$^+$ (indicated as "−" and "+", respectively) in Balb/c mice over time. Two different spectral channels are shown (top and bottom rows). (B) Quantification of accumulation of nanoparticles (designated as "−" and "+") in liver over time, based on signals produced in live animals. (C) Relative quantification of accumulation in organs (24 h, post-mortem). *N* = 3. (D−E) Ex vivo two-photon imaging of mouse liver after intravenous administration of SI-0.2$^+$. (D) 3D reconstruction of nanoparticle distribution across 70 μm depth (Z). (E) Background-corrected intensity ratios for different depths in liver tissue at rest and upon deoxygenation with glucose oxidase/catalase solution (Gox). Asterisks indicate significant difference (independent *t*-test). Scale bar is in micrometers.

excited PLIM or ratiometric-intensity measurements (multimodal detection) such as multiplexed analysis of cell proliferation or cell death, size-dependent oxygenation, or other assays.[42,43,59,60]

To illustrate this, we monitored spheroid oxygenation and cell death (fluorescent stain CellTox Green) (Figure S8, Supporting Information). From day 3 to day 6 of culturing, spheroid average size increased from 370 to 500 μm and the number of dead cells from 10 to 25 per ~0.5 μm thick optical cross-section. The size of spheroid hypoxic core was seen to increase with age and correlate with the number of dead cells. Lifetime distribution across the 6-day-old spheroid becomes broader, reflecting increased O_2 heterogeneity (range 38−200 μm O_2). These O_2 imaging data with the nanoparticle probes shows their usability with 3D tissue models.

***In Vivo* Distribution of the Copolymer Nanoparticles.** To see if the charge of copolymer nanoparticles affects the biodistribution in live animals, we injected SII-0.2$^+$ and SII-0.2$^-$ nanoparticles in the tail vein of a mouse and analyzed live animals on an animal imager at different time points (0−24 h). Due to strong autofluorescence of tissue at excitation wavelengths below 580 nm we were unable to measure poly(fluorene-*alt*-benzothiadiazole) fluorescence but could clearly see Pt(II)−porphyrin (640 nm excitation/780 nm emission). Spectral unmixing (Figure 8 and Figure S9, Supporting Information) revealed predominant accumulation of nanoparticles in the liver, with smaller amounts found in the spleen and lungs, which occurred within 1 h post injection. Upon intraperitoneal injection, however, most of the nanoparticles remained at the point of injection (not shown). Thus, both positively and negatively charged nanoparticles displayed very similar and possibly size-dependent *in vivo* distribution, with retention in the liver (probably due to filtration), which is reminiscent of other types of nanoparticles, gold or polymer-based.[61,62]

Selective accumulation in the liver and other organs can be used for quantitative O_2 measurements *in vivo* or *ex vivo*. We injected SI-0.2$^+$ (analogue of SII-0.2$^+$, which we could measure on two-photon microscope) intravenously, sacrificed the animal, and analyzed *post mortem* liver tissue on a two-photon microscope using excitation at 750 nm (Figure 8E−G). Both the O_2-sensitive (Pt(II)−porphyrin) and reference (polyfluorene) signals were detectable down to 70−100 μm depth. An increase of the ratio signal (650/430) from 0.8 to 1.1 reflects increased tissue deoxygenation over 20 μm depth. Addition of glucose oxidase to the bathing medium, which causes deoxygenation, also increased the ratio signal (Figure 8G, black bars). Thus, copolymer nanoparticles are usable for *ex vivo* imaging

of live animal tissue and can be applied in tissue transplantation, organ viability studies, or diagnostics.

CONCLUSION

Here, we describe a novel type of conjugated polymers that consist of polyfluorene (or poly(fluorene-*alt*-benzothiadiazole) backbone antenna, two types Pt(II)−porphyrin reporter (red and infrared emitting), and pendant charged groups. We found that when forming nanoparticles (30−100 nm) the copolymers display very efficient FRET, high brightness of the O_2-sensitive phosphorescence, and residual emission of the antennae, both under one- and two-photon excitation modes. This makes them attractive cellular O_2-sensitive probes compatible with a broad range of live cell imaging platforms and modes ("multi-modal" probes), especially to two-photon PLIM. At the same time, copolymer nanoparticles can be easily prepared with variety of charged groups (+, −, or ±) to form cationic, anionic or zwitter-ionic structures. This allows them to stain efficiently a broad range of 2D and 3D cell and tissue models−from conventional adherent cells to complex spheroid aggregates. While neither single type of charged nanoparticles can be defined as a "one-for-all" probe we found that the new class of zwitter-ionic nanoparticles shows fast (3 h) and efficient intracellular staining and deep penetration across multiple cell layers in 3D models of HCT116 and PC12 cells.

In conclusion, the copolymer nanoparticles allow for easy optimization of spectral and O_2 sensing properties for particular biological models. Thus, they have high analytical potential for *ex vivo* and *in vivo* imaging of O_2 (or other analytes) on different platforms and applications including regenerative medicine, cancer biology or immunology.

METHODS

Materials. 9,9-Diheptylfluorene-2,7-diboronic acid and 4-*tert*-butylphenylboronic acid were obtained from Frontier Scientific (www.frontiersci.com); (9,9-di(*p*-tolyl)-fluorene-2,7-diyl)diboronic acid, 2,7-dibromo-9,9-di-*p*-tolyl-9*H*-fluorene, and 3,3′-(2,7-dibromo-9*H*-fluorene-9,9-diyl)bis(*N*,*N*-dimethylpropan-1-amine) were from Lumtec (www.lumtec.com.tw); bis(di-*tert*-butyl(4-dimethylaminophenyl)phosphine)dichloropalladium(II) was purchased from Acros (www.fishersci.com). Anhydrous sodium sulfate, tetrahydrofuran, and toluene were from VWR (www.vwr.com), and all other solvents were from Brenntag (www.brenntag.at). pH-Extra, MitoImage-NanoO_2, and MM2 probes were from Luxcel Biosciences (Cork, Ireland). Secondary antibodies labeled with Alexa Fluor 488, LysoTracker Green, Alexa Fluor 488-conjugated cholera toxin, subunit B, transferrin and dextran 10000, and B27 media supplement were from Life Technologies (BioSciences, Dublin, Ireland). Viability Assay kits CellTiter-Glo and CellTox Green were from Promega (MyBio, Ireland). Epidermal growth (EGF) and fibroblast growth (FGF) factors were from Millipore (Cork, Ireland). Rabbit anti-Clathrin heavy chain (no. 2410) and anti-Caveolin-1 (no. 3228) antibodies were obtained from Cell Signaling Technology (Brennan and Co., Dublin). Mouse anti-Cytochrome C antibody (6H2.B4) was from BD Biosciences (Oxford, UK). Hoechst 33342, propidium iodide, Calcein Green AM, 4,7-dibromobenzo[*c*]-1,2,5-thiadiazole, 2,7-dibromofluorene, methyl iodide, and all the other reagents were from Sigma-Aldrich. Standard cell culture grade plasticware was from Sarstedt (Wexford, Ireland) and Corning (VWR, Ireland), and glass bottom minidishes were from MatTek (Ashland, USA). Upright coverglass perfusion chambers (Cat. No. 80226) and glass bottom multiwell chambers were from Ibidi (Martinsried, Germany).

Platinum(II) 5,15-di(pentafluorophenyl)-10,20-di(4-bromophenyl)porphyrin was prepared according to the literature procedure.[31]

Synthesis of dimethyl 3,-(2,7-dibromo-9H-fluorene-9,9-diyl) dipropanoate and platinum(II) *meso*-tetra(4-bromophenyl) tetra-*tert*-butylbenzoporphyrin) PtTPTBPtBu$_4$Br$_4$ are reported in the Supporting Information.

The synthesis of the conjugated polymers and the preparation of the nanoparticles are described for the SI-0.1$^+$/0.1$^-$. The ratio of the precursors for other polymers is reported in the Supporting Information.

Synthesis of the Uncharged Conjugated Polymer Precursor. 108 mg (0.25 mmol) of (9,9-di(*p*-tolyl)-fluorene-2,7-diyl)-diboronic acid, 112 mg (0.25 mmol) of 9,9-diheptylfluorene-2,7-diboronic acid, 152 mg (0.3 mmol) of 2,7-dibromo-9,9-di-*p*-tolyl-9*H*-fluorene, 49 mg (0.1 mmol) of 3,3′-(2,7-dibromo-9*H*-fluorene-9,9-diyl)bis(*N*,*N*-dimethylpropan-1-amine), 49 mg (0.1 mmol) of dimethyl 3,-(2,7-dibromo-9*H*-fluorene-9,9-diyl)dipropanoate, and 9 mg (0.008 mmol) of platinum(II) 5,15-di(pentafluorophenyl)-10,20-di(4-bromophenyl)porphyrin were dissolved in a mixture of 5 mL of toluene and 1.7 mL of tetrahydrofuran in a Schlenk flask. Then, the solutions of 10 mg (0.014 mmol) of bis(di-*tert*-butyl(4-dimethylaminophenyl)phosphine)dichloropalladium(II) in 1 mL of toluene and 276 mg (2 mmol) of potassium carbonate in 1.5 mL of water were added. The sealed flask was stirred overnight at 80 °C. The solution was cooled to room temperature and 10 mg (0.02 mmol) of 2,7-dibromo-9,9-di-*p*-tolyl-9*H*-fluorene were added in order to end-cap the residual boronic acids. After being heated for 1.5 h at 80 °C, the solution was cooled again, 9 mg (0.05 mmol) of 4-*tert*-butylphenylboronic acid was added, and the solution was stirred at 80 °C for 1.5 h. The solution was cooled to room temperature, and 20 mL of dichloromethane and 40 mL of water were added. The organic phase was dried over anhydrous sodium sulfate. The solution of the polymer was added dropwise under stirring to 120 mL of methanol in order to remove oligomers. The precipitate was collected, washed with methanol, and dried in an oven at 60 °C. Yield: 156 mg of the reddish powder.

Synthesis of the Charged Polymer and Preparation of the Nanoprobes. The polymer (50 g) was dissolved in 2.5 mL of water-free toluene in a Schlenk flask. Twenty-four mg of potassium carbonate and 6.1 μL of methyl iodide were added under argon flow. The flask was sealed, and the solution was stirred for 4 h at 80 °C. After the completion of the reaction the solvent was removed under reduced pressure, and the resulting polymer washed several times with water. The polymer was dissolved in 5 mL of tetrahydrofuran, and 100 μL of 1 M NaOH were added. The solution was stirred for 1 h at 40 °C and then diluted with a mixture of 7.5 mL of tetrahydrofuran and 12.5 mL of acetone. This solution was placed in a 150 mL beaker and 100 mL of water was rapidly added inside (within 2−3 s) under vigorous stirring (800 rpm). The organic solvents were removed under reduced pressure, and the nanoparticle dispersion was concentrated to 50 mL. Prior to storage, the dispersion was centrifuged (6000 rpm) to remove some aggregates formed during the solvent evaporation.

Spectral Measurements. Luminescence excitation and emission spectra were acquired on a Fluorolog 3 fluorescence spectrometer from Horiba (www.horiba.com) equipped with an NIR-sensitive photomultiplier R2658 from Hamamatsu (www.hamamatsu.com). The luminescence quantum yields were determined relative to platinum(II) octaethylporphyrin in toluene (Φ = 0.405)[63] in the case of the SI series, MM2, and

$NanO_2$ (λ_{exc} = 380 nm) or relative to platinum(II) tetraphenyltetrabenzoporphyrin in toluene (Φ = 0.51)[64] in the case of the SII series and $NanO_2$–IR (λ_{exc} = 435 and 620 nm) according to Crossby and Demas.[65] The dispersions of the nanobeads were deoxygenated by adding 5 wt % glucose and 0.5 mg of glucose oxidase as a catalyst, whereas the solutions of the reference dyes were deoxygenated by bubbling nitrogen through the screw-cap cuvette from Hellma (www.hellma-analytics.com). Luminescence decay times were measured on a Fluorolog 3 equipped with a DeltaHub module for single photon counting measurements. NanoLED (λ_{max} 453 nm) and SpectraLED (λ_{max} 392 nm) from Horiba were used for the excitation. GPC measurements for determination of molecular weights and the polydispersity index (PDI) of the polymers were performed in tetrahydrofuran (THF) using a Merck Hitachi L6000 pump, separation columns of Polymer Standards Service (5 μm grade size), and a refractive-index detector from Wyatt Technology. Polystyrene standards purchased from Polymer Standard Service were used for calibration. The size of the nanobeads was determined with a particle size analyzer Zetasizer Nano ZS from Malvern (www.malvern.com).

Cell Culture. Mouse embryonic fibroblast (MEF), rat pheochromocytoma (PC12), and human colorectal carcinoma HCT116 cells from ATCC (Manassas, VA) were handled as described previously.[42,59] PC12 cell aggregates (sPC12 cells) were handled as described previously.[59] Spheroids from HCT116 cells (sHCT116) were formed by seeding in "spheroid formation medium" (Phenol red-free DMEM, supplemented with 10 mM Glc, 1 mM sodium pyruvate, 2 mM L-glutamine, 1% penicillin–streptomycin, 10 mM HEPES–Na, pH 7.2, 2% B27, 20 ng/mL of FGF, 10 ng/mL of EGF) and culturing in 25 cm^2 tissue culture flasks (low attachment grade) for 3–5 days. Alternatively, cells were seeded in regular growth medium (McCoy's 5A supplemented with 10% FBS, 1% penicillin–streptomycin, 10 mM HEPES–Na, pH 7.2) on Lipidure-coat plates (Amsbio, Oxford, UK) at concentration 1,000/well and cultured for 3–5 days.

For microplate reader-based measurements (cell staining efficacy, ATP, ECA viability assays), cells were seeded on collagen IV-coated[66] 96-well plates at 50–75% confluence day before measurements. For widefield fluorescence microscopy (cell staining kinetics, optimization of cell loading) cells were seeded on sterile multiwell silicone coverglass bottom units ("FlexiPERM", Greiner Bio One), precoated with mixture of collagen IV-poly-D-lysine[66] at 30–50% confluence 1 day before experiment. For two-photon measurements cells were seeded in collagen IV-poly-D-lysine coated upright perfusion chambers (Ibidi, 80226), loaded with nanoparticles, washed with PBS, fixed with 4% paraformaldehyde, washed, and stored in PBS (4 °C). For all other imaging experiments, cells were grown on collagen IV-poly-D-lysine[66]-coated 35 mm glass bottom (MatTek) or plastic bottom (Sarstedt) dishes.

The staining with nanoparticles was achieved by incubation at indicated concentration (0–20 μg/mL), at indicated time points in regular growth medium for 0–24 h, followed by 2–3 washes with growth medium. Imaging and related measurements were normally performed in phenol red-free DMEM (Sigma D5030) supplemented with 10 mM Glc, 1 mM sodium pyruvate, 2 mM L-glutamine, and 10 mM HEPES-Na, pH 7.2.

The toxicity of nanoparticles was evaluated by loading of adherent MEF cells with nanoparticles for 16 h with indicated concentrations, washing and then analysis of total cellular ATP (CellTiter-Glo assay) and extracellular acidification (ECA, using pH-Extra probe assay, unsealed samples) as described before.[67] For analysis of membrane integrity, MEF cells loaded with nanoparticles were stained with CellTox Green reagent (0.05%, 10 min) and analyzed on widefield fluorescence microscope.

Immunofluorescence experiments were performed as follows: MEF cells grown on glass-bottom collagen–PDL-coated 12-well slides were loaded with nanoparticles (5 μg/mL, 16 h), washed twice with medium, then with PBS (two times), fixed with 4% paraformaldehyde (30 min, rt), washed with PBS (two times), permeabilised with 0.1% Triton X100 (5 min, rt), and then incubated with primary and secondary antibodies as described before.[43]

Microscopy. Measurements of cell staining kinetics, analysis of subcellular localization of nanoparticles (immunofluorescence) and "in-cell" O_2 calibrations were performed on custom-made widefield fluorescence PLIM microscope, based on Axiovert 200 (Carl Zeiss) inverted microscope equipped with 40*x*/1.3 Plan Neofluar and 100*x*/1.4 Plan Apochromat oil-immersion objectives, O_2, CO_2 and humidity climate control chamber (PeCon), pulsed LED excitation module (390, 470, and 590 nm) and gated CCD camera.[43] Analysis of subcellular localization (colocalization with Calcein Green) and staining efficiency of sPC12 and sHCT116 3D models were performed on upright microscope Axio Examiner Z1 (Carl Zeiss)[43] equipped with 20*x*/1.0 and 63*x*/1.0 W-Plan Apochromat dipping objectives, heated stage (T= 37 °C) with motorized *Z*-axis control, DCS-120 confocal TCSPC scanner (Becker and Hickl GmbH), two photon counting detectors R10467U-40 (>30% quantum efficiency at 400–700 nm) and R10467U-50 (>10% quantum efficiency at 500–880 nm) and dedicated TCSPC operating software. (Becker and Hickl GmbH). Nanoparticles MM2, NanO2, and different SI nanoparticles were excited using 405 nm picosecond diode laser BDL-SMC (Becker and Hickl GmbH) with emissions collected at 635–675 nm (Pt(II)–porphyrin) and 428–468 nm (polyfluorene). Calcein Green was excited using picosecond supercontinuum laser SC400–4 (Fianium, UK) at 488 nm with emission collected at 512–536 nm. Nanoparticles SII were excited using laser SC400–4 at either 488 or 632 nm with emissions collected at 512–536 nm (poly(fluorene-*alt*-benzothiadiazole)) or 750–810 nm (Pt(II)–porphyrin). PLIM and FLIM measurements were performed as described before.[42,68]

Two-photon imaging of fixed MEF cells was performed on an upright Zeiss 710 NLO microscope equipped with 100*x*/1.45 alpha Plan Fluar oil immersion objective, Coherent Chameleon Vision II laser and ZEN ver. 2009 software. The emission was collected using beam splitter 690 nm, beam splitter 590 nm and bandpass 625–655 nm and short pass 480 nm filter (MM2, PA2, SI-0.2^+, SI-0.1^+/0.1^- nanoparticles) or a mirror and filter 505–550 nm for the SII-0.2^+ nanoparticles. Zoom was set to a pixel size of 0.17 μm and pixel dwell time was 1.58 μs.

Two-photon *ex vivo* imaging of liver was performed on inverted laser scanning Nikon A1R MP microscope equipped with Ti-sapphire femtosecond Mai Tai laser (Spectra Physics), 20*x*/0.75 Plan Apochromat objective, temperature (set at 37 °C) and CO_2 control and controlled using NIS-elements AR (ver. 4.13) software. SI-0.2^+ nanoparticles were excited at 750 nm (1.5% laser power). The emissions were collected using beam splitter 760 nm and bandpass 663–738 nm (Pt(II)–porphyrin) and 425–475 nm (polyfluorene) filters.

***In Vivo* Distribution Experiments and *ex Vivo* Imaging of Liver.** All of the procedures with animals were performed in accordance with the "Guidelines on Laboratory Practices in the Russian Federation" adopted by the Ministry of Health of the Russian Federation (Order 267, 19 June 2003). The experimental protocol was approved by Bioethics Committee of Pirogov Russian National Research Medical University.

Adult female mice (Balb/c) with average weight 20 g were anesthetized by Izoflurane and placed in Ivis Spectrum CT chamber (PerkinElmer). After recording of background fluorescence level with autoexposure with different filter configurations (ex/em (nm): 500/540, 500/560, 500/580, 500/600, 500/620, 500/760, 500/780, 500/800, 500/820, 500/840, 640/760, 640/780, 640/800, 640/820, 640/840) SII-0.2^+ and SII-0.2^- probes were injected in a tail vein at a dose 50 μg per mouse (approximately 2.5 mg/kg). 10, 30 min, 1, 2, and 24 h after injection the nanoparticle fluorescence was detected using the same filter configuration. After that, mice were sacrificed. The detection of nanoparticle fluorescence was then performed post-mortem with removed abdominal wall and with extracted organs. Quantitative analysis of fluorescence values was performed using "Living imaging" Software ver. 4.4 (PerkinElmer).

For *ex vivo* liver imaging, the mouse was injected with SI-0.2^+ as above, sacrificed 2 h after injection, then liver was quickly extracted, soaked in Hanks' Balanced Salt Solution and imaged at two-photon microscope at 37 °C. To deplete O_2 in the sample, the solution of 56 g/L glucose oxidase (G2133, Sigma),

3.4 g/L catalase (C40, Sigma) in 8 mM Tris, 40 mM NaCl, and 8% dextrose, pH 8 was applied at a final concentration of 2%.

Data Assessment. Plate reader data represent averaged values with standard deviation shown as error bars from >6 replicates (N indicated in figure legends). Cell loading, immunofluorescence, and all the other microscopy imaging experiments were performed in triplicate with the data presented as averaged intensity values from 6 to 10 independently selected ROI (N indicated in figure legends). Where appropriate, an independent *t*-test was performed with confidence levels $P = 0.5$ and 0.05 accepted as significant. 2D matrices of intensity and phosphorescence lifetime images were generated using SPCImage software (Becker and Hickl GmbH) using monoexponential fitting, tail-enhanced fit ($\chi^2 < 1.5$) and then processed in Microsoft Excel software.

Conflict of Interest: The authors declare no competing financial interest.

Acknowledgment. This work was supported by the Science Foundation Ireland (SFI) (Grant Nos. 13/SIRG/2144 (R.I.D.) and 12/RC/2276 (D.B.P.)), European Research Council, project "Oxygen" No. 267233 (S.M.B.), and Russian Scientific Foundation (grant 14-14-00882 (V.P.B.)). We are grateful to A. O'Neill, J. Jenkins, Dr. A. Kondrashina, and P. Melnikov for technical assistance.

Supporting Information Available: Supplementary figures S1–S9, supplementary tables S1–S2, and supplementary experimental procedures. This material is available free of charge *via* the Internet at http://pubs.acs.org.

REFERENCES AND NOTES

1. Wang, X.-d.; Wolfbeis, O. S. Optical Methods for Sensing and Imaging Oxygen: Materials, Spectroscopies and Applications. *Chem. Soc. Rev.* **2014**, *43*, 3666–3761.
2. Papkovsky, D. B.; Dmitriev, R. I. Biological Detection by Optical Oxygen Sensing. *Chem. Soc. Rev.* **2013**, *42*, 8700–8732.
3. Frederiksen, M. S.; Glud, R. N. Oxygen Dynamics in the Rhizosphere of Zostera Marina: a Two-Dimensional Planar Optode Study. *Limnol. Oceanogr.* **2006**, *51*, 1072–1083.
4. Glud, R.; Ramsing, N. B.; Gundersen, J. K.; Klimant, I. Planar Optodes, a New Tool for Fine Scale Measurements of Two-Dimensional O2 Distribution in Benthic Communities. *Mar. Ecol.: Prog. Ser.* **1996**, *140*, 217–226.
5. Klimant, I.; Meyer, V.; Kühl, M. Fiber-Optic Oxygen Microsensors, a New Tool in Aquatic Biology. *Limnol. Oceanogr.* **1995**, *40*, 1159–1165.
6. Wolfbeis, O. S. Sensor Paints. *Adv. Mater.* **2008**, *20*, 3759–3763.
7. Aylott, J. W. Optical Nanosensors—an Enabling Technology for Intracellular Measurements. *Analyst* **2003**, *128*, 309–312.
8. Borisov, S. M.; Klimant, I. Optical Nanosensors—Smart Tools in Bioanalytics. *Analyst* **2008**, *133*, 1302–1307.
9. Dmitriev, R.; Papkovsky, D. Intracellular Probes for Imaging Oxygen Concentration: How Good are They? *Methods Appl. Fluoresc.* **2015**in press.
10. Doane, T. L.; Burda, C. The Unique Role of Nanoparticles in Nanomedicine: Imaging, Drug Delivery and Therapy. *Chem. Soc. Rev.* **2012**, *41*, 2885–2911.
11. Ruedas-Rama, M. J.; Walters, J. D.; Orte, A.; Hall, E. A. Fluorescent Nanoparticles for Intracellular Sensing: a Review. *Anal. Chim. Acta* **2012**, *751*, 1–23.
12. Devor, A.; Sakadzic, S.; Srinivasan, V. J.; Yaseen, M. A.; Nizar, K.; Saisan, P. A.; Tian, P.; Dale, A. M.; Vinogradov, S. A.; Franceschini; et al. Frontiers in Optical Imaging of Cerebral Blood Flow and Metabolism. *J. Cereb. Blood Flow Metab.* **2012**, *32*, 1259–1276.
13. Provenzano, P. P.; Eliceiri, K. W.; Keely, P. J. Multiphoton Microscopy and Fluorescence Lifetime Imaging Microscopy (FLIM) to Monitor Metastasis and the Tumor Microenvironment. *Clin. Exp. Metastasis* **2009**, *26*, 357–370.
14. Roussakis, E.; Spencer, J. A.; Lin, C. P.; Vinogradov, S. A. Two-Photon Antenna-Core Oxygen Probe with Enhanced Performance. *Anal. Chem.* **2014**, *86*, 5937–5945.
15. Albenberg, L.; Esipova, T. V.; Judge, C. P.; Bittinger, K.; Chen, J.; Laughlin, A.; Grunberg, S.; Baldassano, R. N.; Lewis, J. D.; Li, H.; et al. Correlation Between Intraluminal Oxygen Gradient And Radial Partitioning of Intestinal Microbiota in Humans and Mice. *Gastroenterology* **2014**, *147*, 1055–1063.e8.
16. Spencer, J. A.; Ferraro, F.; Roussakis, E.; Klein, A.; Wu, J.; Runnels, J. M.; Zaher, W.; Mortensen, L. J.; Alt, C.; Turcotte, R.; et al. Direct Measurement of Local Oxygen Concentration in The Bone Marrow of Live Animals. *Nature* **2014**, *508*, 269–273.
17. He, G. S.; Tan, L.-S.; Zheng, Q.; Prasad, P. N. Multiphoton Absorbing Materials: Molecular Designs, Characterizations, and Applications. *Chem. Rev.* **2008**, *108*, 1245–1330.
18. Pawlicki, M.; Collins, H. A.; Denning, R. G.; Anderson, H. L. Two-Photon Absorption and the Design of Two-Photon Dyes. *Angew. Chem., Int. Ed.* **2009**, *48*, 3244–3266.
19. Finikova, O. S.; Lebedev, A. Y.; Aprelev, A.; Troxler, T.; Gao, F.; Garnacho, C.; Muro, S.; Hochstrasser, R. M.; Vinogradov, S. A. Oxygen Microscopy by Two-Photon-Excited Phosphorescence. *ChemPhysChem* **2008**, *9*, 1673–1679.
20. Ray, A.; Koo Lee, Y.-E.; Epstein, T.; Kim, G.; Kopelman, R. Two-Photon Nano-PEBBLE Sensors: Subcellular pH Measurements. *Analyst* **2011**, *136*, 3616–3622.
21. Rao, A. S.; Kim, D.; Wang, T.; Kim, K. H.; Hwang, S.; Ahn, K. H. Reaction-Based Two-Photon Probes for Mercury Ions: Fluorescence Imaging with Dual Optical Windows. *Org. Lett.* **2012**, *14*, 2598–2601.
22. Esipova, T. V.; Vinogradov, S. A. Synthesis of Phosphorescent Asymmetrically Pi-Extended Porphyrins for Two-Photon Applications. *J. Org. Chem.* **2014**, *79*, 8812–8825.
23. Lee, Y.-E. K.; Kopelman, R.; Smith, R. Nanoparticle PEBBLE Sensors in Live Cells and *in vivo*. *Annu. Rev. Anal. Chem.* **2009**, *2*, 57.
24. Quaranta, M.; Borisov, S. M.; Klimant, I. Indicators for Optical Oxygen Sensors. *Bioanal. Rev.* **2012**, *4*, 115–157.
25. Holst, G.; Kohls, O.; Klimant, I.; König, B.; Kühl, M.; Richter, T. A Modular Luminescence Lifetime Imaging System for Mapping Oxygen Distribution in Biological Samples. *Sens. Actuators, B* **1998**, *51*, 163–170.
26. Becker, W. Fluorescence Lifetime Imaging – Techniques and Applications. *J. Microsc.* **2012**, *247*, 119–136.
27. Zhang, G.; Palmer, G. M.; Dewhirst, M. W.; Fraser, C. L. A Dual-Emissive-Materials Design Concept Enables Tumour Hypoxia Imaging. *Nat. Mater.* **2009**, *8*, 747–751.
28. Feng, Y.; Cheng, J.; Zhou, L.; Zhou, X.; Xiang, H. Ratiometric Optical Oxygen Sensing: a Review in Respect of Material Design. *Analyst* **2012**, *137*, 4885–4901.
29. Meier, R. J.; Fischer, L. H.; Wolfbeis, O. S.; Schäferling, M. Referenced Luminescent Sensing and Imaging with Digital Color Cameras: a Comparative Study. *Sens. Actuators, B* **2013**, *177*, 500–506.
30. Wang, X.-d.; Gorris, H. H.; Stolwijk, J. A.; Meier, R. J.; Groegel, D. B.; Wegener, J.; Wolfbeis, O. S. Self-Referenced RGB Colour Imaging of Intracellular Oxygen. *Chem. Sci.* **2011**, *2*, 901–906.
31. Xiang, H.; Zhou, L.; Feng, Y.; Cheng, J.; Wu, D.; Zhou, X. Tunable Fluorescent/Phosphorescent Platinum (II) Porphyrin–Fluorene Copolymers for Ratiometric Dual Emissive Oxygen Sensing. *Inorg. Chem.* **2012**, *51*, 5208–5212.
32. Amelia, M.; Lavie-Cambot, A.; McClenaghan, N. D.; Credi, A. A Ratiometric Luminescent Oxygen Sensor Based on a Chemically Functionalized Quantum Dot. *Chem. Commun.* **2011**, *47*, 325–327.
33. Yoshihara, T.; Yamaguchi, Y.; Hosaka, M.; Takeuchi, T.; Tobita, S. Ratiometric Molecular Sensor for Monitoring Oxygen Levels in Living Cells. *Angew. Chem.* **2012**, *124*, 4224–4227.
34. Shi, H.; Ma, X.; Zhao, Q.; Liu, B.; Qu, Q.; An, Z.; Zhao, Y.; Huang, W. Ultrasmall Phosphorescent Polymer Dots for Ratiometric Oxygen Sensing and Photodynamic Cancer Therapy. *Adv. Funct. Mater.* **2014**, *24*, 4823–4830.

35. Grimsdale, A. C.; Leok Chan, K.; Martin, R. E.; Jokisz, P. G.; Holmes, A. B. Synthesis of Light-Emitting Conjugated Polymers for Applications in Electroluminescent Devices. *Chem. Rev.* **2009**, *109*, 897–1091.
36. Facchetti, A. π-Conjugated Polymers for Organic Electronics and Photovoltaic Cell Applications. *Chem. Mater.* **2010**, *23*, 733–758.
37. Zhou, H.; Yang, L.; You, W. Rational Design of High Performance Conjugated Polymers for Organic Solar Cells. *Macromolecules* **2012**, *45*, 607–632.
38. McQuade, D. T.; Pullen, A. E.; Swager, T. M. Conjugated Polymer-Based Chemical Sensors. *Chem. Rev.* **2000**, *100*, 2537–2574.
39. Zhu, C.; Liu, L.; Yang, Q.; Lv, F.; Wang, S. Water-Soluble Conjugated Polymers for Imaging, Diagnosis, and Therapy. *Chem. Rev.* **2012**, *112*, 4687–4735.
40. Li, K.; Liu, B. Polymer-Encapsulated Organic Nanoparticles for Fluorescence and Photoacoustic Imaging. *Chem. Soc. Rev.* **2014**, *43*, 6570–6597.
41. Wu, C.; Bull, B.; Christensen, K.; McNeill, J. Ratiometric Single-Nanoparticle Oxygen Sensors for Biological Imaging. *Angew. Chem., Int. Ed.* **2009**, *48*, 2741–2745.
42. Dmitriev, R. I.; Borisov, S. M.; Kondrashina, A. V.; Pakan, J. M. P.; Anilkumar, U.; Prehn, J. H. M.; Zhdanov, A. V.; McDermott, K. W.; Klimant, I.; Papkovsky, D. B. Imaging Oxygen in Neural Cell and Tissue Models by Means of Anionic Cell-Permeable Phosphorescent Nanoparticles. *Cell. Mol. Life Sci.* **2015**, *72*, 367–381.
43. Dmitriev, R. I.; Zhdanov, A. V.; Nolan, Y. M.; Papkovsky, D. B. Imaging of Neurosphere Oxygenation with Phosphorescent Probes. *Biomaterials* **2013**, *34*, 9307–9317.
44. Nichols, A. J.; Roussakis, E.; Klein, O. J.; Evans, C. L. Click-Assembled, Oxygen-Sensing Nanoconjugates for Depth-Resolved, Near-Infrared Imaging in a 3 D Cancer Model. *Angew. Chem., Int. Ed.* **2014**, *53*, 3671–3674.
45. Pampaloni, F.; Reynaud, E. G.; Stelzer, E. H. The Third Dimension Bridges the Gap between Cell Culture and Live Tissue. *Nat. Rev. Mol. Cell Biol.* **2007**, *8*, 839–845.
46. Borisov, S. M.; Mayr, T.; Mistlberger, G.; Waich, K.; Koren, K.; Chojnacki, P.; Klimant, I. Precipitation as a Simple and Versatile Method for Preparation of Optical Nanochemosensors. *Talanta* **2009**, *79*, 1322–1330.
47. Kondrashina, A. V.; Dmitriev, R. I.; Borisov, S. M.; Klimant, I.; O'Brien, I.; Nolan, Y. M.; Zhdanov, A. V.; Papkovsky, D. B. A Phosphorescent Nanoparticle-Based Probe for Sensing and Imaging of (Intra)Cellular Oxygen in Multiple Detection Modalities. *Adv. Funct. Mater.* **2012**, *22*, 4931–4939.
48. Fercher, A.; Borisov, S. M.; Zhdanov, A. V.; Klimant, I.; Papkovsky, D. B. Intracellular O2 Sensing Probe Based on Cell-Penetrating Phosphorescent Nanoparticles. *ACS Nano* **2011**, *5*, 5499–5508.
49. Tsytsarev, V.; Arakawa, H.; Borisov, S.; Pumbo, E.; Erzurumlu, R. S.; Papkovsky, D. B. In Vivo Imaging of Brain Metabolism Activity Using a Phosphorescent Oxygen-Sensitive Probe. *J. Neurosci. Methods* **2013**, *216*, 146–151.
50. Keivanidis, P. E.; Laquai, F.; Robertson, J. W.; Baluschev, S.; Jacob, J.; Müllen, K.; Wegner, G. Electron-Exchange-Assisted Photon Energy Up-Conversion in Thin Films Of π-Conjugated Polymeric Composites. *J. Phys. Chem. Lett.* **2011**, *2*, 1893–1899.
51. Carraway, E.; Demas, J.; DeGraff, B.; Bacon, J. Photophysics and Photochemistry of Oxygen Sensors Based on Luminescent Transition-Metal Complexes. *Anal. Chem.* **1991**, *63*, 337–342.
52. Wu, C.; Szymanski, C.; Cain, Z.; McNeill, J. Conjugated Polymer Dots for Multiphoton Fluorescence Imaging. *J. Am. Chem. Soc.* **2007**, *129*, 12904–12905.
53. Yao, S.; Ahn, H.-Y.; Wang, X.; Fu, J.; Van Stryland, E. W.; Hagan, D. J.; Belfield, K. D. Donor– Acceptor– Donor Fluorene Derivatives for Two-Photon Fluorescence Lysosomal Imaging. *J. Org. Chem.* **2010**, *75*, 3965–3974.
54. Lebedev, A. Y.; Troxler, T.; Vinogradov, S. A. Design of Metalloporphyrin-Based Dendritic Nanoprobes for Two-Photon Microscopy of Oxygen. *J. Porphyrins Phthalocyanines* **2008**, *12*, 1261–1269.
55. Ivanov, A. I. Pharmacological Inhibition of Endocytic Pathways: Is It Specific Enough to Be Useful? In *Exocytosis and Endocytosis*; Ivanov, A. I., Ed.; Springer: New York, 2008; pp 15–33.
56. Canton, I.; Battaglia, G. Endocytosis at the Nanoscale. *Chem. Soc. Rev.* **2012**, *41*, 2718–2739.
57. Wang, X.-H.; Peng, H.-S.; Yang, L.; You, F.-T.; Teng, F.; Hou, L.-L.; Wolfbeis, O. S. Targetable Phosphorescent Oxygen Nanosensors for the Assessment of Tumor Mitochondrial Dysfunction by Monitoring the Respiratory Activity. *Angew. Chem.* **2014**, *53*, 12471–12475.
58. Shin, S. J.; Beech, J. R.; Kelly, K. A. Targeted Nanoparticles in Imaging: Paving the Way for Personalized Medicine in the Battle Against Cancer. *Integr. Biol.* **2013**, *5*, 29–42.
59. Dmitriev, R. I.; Kondrashina, A. V.; Koren, K.; Klimant, I.; Zhdanov, A. V.; Pakan, J. M. P.; McDermott, K. W.; Papkovsky, D. B. Small Molecule Phosphorescent Probes for O2 Imaging in 3D Tissue Models. *Biomater. Sci.* **2014**, *2*, 853–866.
60. Dmitriev, R.; Papkovsky, D. Multi-Parametric O2 Imaging in Three-Dimensional Neural Cell Models with the Phosphorescent Probes. In *Neuronal Cell Death*, Lossi, L.; Merighi, A., Eds. Springer: New York, 2015; Vol. 1254, pp 55–71.
61. Nel, A. E.; Mädler, L.; Velegol, D.; Xia, T.; Hoek, E. M.; Somasundaran, P.; Klaessig, F.; Castranova, V.; Thompson, M. Understanding Biophysicochemical Interactions at the Nano–Bio Interface. *Nat. Mater.* **2009**, *8*, 543–557.
62. He, C.; Hu, Y.; Yin, L.; Tang, C.; Yin, C. Effects of Particle Size and Surface Charge on Cellular Uptake and Biodistribution of Polymeric Nanoparticles. *Biomaterials* **2010**, *31*, 3657–3666.
63. Bansal, A.-K.; Holzer, W.; Penzkofer, A.; Tsuboi, T. Absorption and Emission Spectroscopic Characterization of Platinum-Octaethyl-Porphyrin (PtOEP). *Chem. Phys.* **2006**, *330*, 118–129.
64. Borisov, S.; Nuss, G.; Haas, W.; Saf, R.; Schmuck, M.; Klimant, I. New NIR-emitting Complexes of Platinum (II) and Palladium (II) with Fluorinated Benzoporphyrins. *J. Photochem. Photobiol., A* **2009**, *201*, 128–135.
65. Crosby, G. A.; Demas, J. N. Measurement of Photoluminescence Quantum Yields. Review. *J. Phys. Chem.* **1971**, *75*, 991–1024.
66. Zhdanov, A. V.; Dmitriev, R. I.; Hynes, J.; Papkovsky, D. B. Chapter Ten - Kinetic Analysis of Local Oxygenation and Respiratory Responses of Mammalian Cells Using Intracellular Oxygen-Sensitive Probes and Time-Resolved Fluorometry. In *Methods in Enzymology*; Lorenzo, G., Guido, K., Eds.; Academic Press: New York, 2014; Vol. 542, pp 183–207.
67. Zhdanov, A. V.; Favre, C.; O'Flaherty, L.; Adam, J.; O'Connor, R.; Pollard, P. J.; Papkovsky, D. B. Comparative Bioenergetic Assessment of Transformed Cells Using a Cell Energy Budget Platform. *Integrative Biol.* **2011**, *3*, 1135–1142.
68. Aigner, D.; Dmitriev, R.; Borisov, S. M.; Papkovsky, D. B.; Klimant, I. pH-Sensitive Perylene Bisimide Probes for Live Cell Fluorescence Lifetime Imaging. *J. Mater. Chem. B* **2014**, *2*, 6792–6801.